ECS Transactions, 35 (1) 1513-1528 (2011)
10.1149/1.3570136 ©The Electrochemical Society

Electrooxidation of Reformate Gases at Model Anodes

A. Weber[1], A. Utz[1], J. Joos[1], E. Ivers-Tiffée[1,3], H. Störmer[2], D. Gerthsen[2,3]
V. Yurkiv[4,5], H.-R. Volpp[4], W. G. Bessler[5,6]

[1] Institut für Werkstoffe der Elektrotechnik (IWE)
[2] Laboratorium für Elektronenmikroskopie (LEM)
[3] DFG Center for Functional Nanostructures (CFN)
Karlsruher Institut für Technologie (KIT), D-76131 Karlsruhe, Germany
[4] Institute of Physical Chemistry, Heidelberg University, Heidelberg, Germany
[5] German Aerospace Centre (DLR), Institute of Technical Thermodynamics
Stuttgart, Germany
[6] Institute of Thermodynamics and Thermal Engineering (ITW), Universität Stuttgart
Stuttgart, Germany

This paper summarizes the experimental and modeling results concerning the electrooxidation of hydrogen and carbon monoxide, the main oxidizable compounds in reformates, at patterned nickel anodes on polycrystalline yttria stabilized zirconia electrolytes. The line specific resistance of the three phase boundary was evaluated within a wide range of gas compositions and temperature. The investigations showed that microstructural stability, impurities, accelerated degradation and reversible dynamic changes are key issues which have to be considered. Elementary kinetic models, parameterized with literature data, temperature-programmed desorption and reaction and quantum chemical calculation results were in excellent agreement with the experimental data. For the first time it could be shown that the line specific resistance values evaluated by means of patterned anodes are applicable in homogenized and space resolved models for cermet anodes.

Introduction

In order to allow experimentally and theoretically more detailed investigations of the electrochemical processes at the three phase boundary (TPB), various types of model anodes as micropatterned, point and mesh type electrodes have been used (1-6). These systems are expected to have geometrically well-defined active surfaces and two- and three-phase boundaries. Furthermore there is no complex coupling of TPB-reactions, gas diffusion and bulk transport as it is unavoidable in technical anode structures (7). Still, numerous studies have shown the high complexity of the electrochemical behavior of these geometrically simple systems. In order to allow a mechanistic interpretation of observed electrochemical behavior in terms of reaction pathways and rate-determining steps, anode models have been developed. This includes both atomistic quantum chemical models and mean-field kinetic models. These models allow a detailed assessment of the interaction of charge-transfer reactions with surface and bulk transport in the geometrically confined regions of the model electrode.

Model anodes are characterized by their well-defined microscale geometry. For patterned anodes, metal patterns are photolithographically applied on a solid electrolyte

substrate. This technique allows well-defined contact areas and high TPB lengths l_{TPB}. Preparation can either be realized by metal etching or metal liftoff, as described in (8,9). Metal thickness varies from 0.1–2 µm, with pattern widths in the range of 5–50 µm. This results in absolute TPB lengths in the range of l_{TPB} = 1 ... 10 m within a 1 cm^2 electrode.

Electrochemical characterization of patterned anodes is usually performed by IV-characteristics and electrochemical impedance spectroscopy. The latter is a powerful tool to separate individual electrode processes. The variation of parameters as gas composition, temperature and polarization voltage provides information about parameter dependencies and should enable us to determine the physical origin of the electrode processes. Several studies exist for the characterization in H_2-H_2O atmosphere (1-6), while literature on the characterization in CO-CO_2 atmosphere is sparse (5,10,11). Despite of the well-defined geometry, the analysis of results from electrochemical characterization of patterned anodes in H_2-H_2O anodes revealed strong deviations with respect to absolute line specific resistance (LSR) values as well as parameter dependencies (6), impeding the evaluation of modeling studies of the elementary reaction mechanism. These deviations are potentially caused by instabilities of the Ni thin film (5), impurities at the TPB (12) or errors induced by an inappropriate use of reference electrodes (13). Therefore detailed stability and impurity analyses of patterned anodes are indispensible (6,14).

In order to allow a mechanistic interpretation of observed electrochemical behavior in terms of reaction pathways and rate-determining steps, numerical anode models have been developed. This includes both atomistic quantum chemical models (15) and mean-field kinetic models (16). These models allow a detailed assessment of the interaction of charge-transfer reactions with surface and bulk transport in the geometrically confined regions of the model electrode.

In this paper, our results on experimental and modeling investigations concerning the electrooxidation of the oxidizable compounds (H_2 and CO) of reformate gases at model anodes are summarized. It will be shown that a careful experimental analysis of model anodes is the basis for a detailed elementary kinetic modeling of TPB reactions as well as for homogenized and spatially resolved models of cermet anodes.

Experimental

Processing of Patterned Ni Anodes

As pointed out in one of our previous papers (9), there are various methods and procedures to fabricate patterned anodes. In this study results of patterned Ni-anodes deposited on 8.5 mol% polycrystalline Y_2O_3-stabilized ZrO_2 (YSZ) substrates (Itochu Ceratec Corp., Japan) by a lift-off process are discussed. The design of the 800 nm thick Ni layer was composed of parallel stripes with a width of 8 to 25 µm, yielding a TPB length between 1 to 8 m. Two stripes at the ends ensure proper contacting of the patterned Ni anodes. Whereas in previous study no impact of the stripe and spacing width was observed (6), the thickness of 800 nm is required to ensure the stability of the structure during characterization at temperatures of up to 800 °C in reducing atmosphere (17).

Microstructural Characterization

As discussed in (5) the microstructural stability is a key issue for patterned anodes. Therefore the samples were analyzed by scanning electron microscopy (SEM: Zeiss 1540 XB) before and after electrochemical characterization (6,18). In addition, the TBP and the nickel / YSZ interface of selected samples was analyzed by transmission electron microscopy (TEM: FEI Titan 80-300) to detect impurity phases as described in (19).

Impurity Analysis

In order to assess the impurity composition and concentration on the patterned Ni anodes, detailed impurity analysis has been performed at Risø DTU National Laboratory for Sustainable Energy by means of Atomic Force Microscopy (AFM: DME Danish Micro Engineering DualScope atomic force microscope), Time-of-Flight Secondary Ion Mass Spectrometry (TOF-SIMS: ION-TOF GmbH, Germany) and X-ray Photoelectron Spectroscopy (XPS: Thermo Fisher Scientific, UK). Details about the analysis procedures are given in (14,19). YSZ-substrates, patterned Ni anodes after electrochemical characterization and similar samples after removing the Ni electrode in an acidic solution of HNO_3 have been investigated. Hence it is possible to assess all regions of interest: i) the YSZ surface, ii) the Ni surface, iii) the electrode-electrolyte interface between YSZ and Ni, and iv) the TPB.

Electrochemical Characterization

To circumvent the unavoidable distortions of the impedance caused by reference electrodes (13), an electrochemically well defined Ni/8YSZ cermet anode exhibiting an at least 2 orders of magnitude lower polarization resistance was chosen as the counter electrode. The Ni/YSZ counter electrode was screen-printed following the procedure described by Sonn et al. (20). The electrochemical characteristics of this electrode are summarized in the same paper. This counter electrode was applied before preparation of the Ni patterned anodes, as sintering and reduction of this anode require the highest temperatures.

The samples were contacted either by Ni meshes or a special contact block, an additional weight of 18 g on top ensures the electrical contact (6,11). The sample holder was then placed in a gastight Al_2O_3 chamber where the sample was purged with the appropriate fuel gas composition on both sides. The fuel gas composition was controlled by mass flow controllers with a total gas flow of 100 – 300 ml/min; N_2 was used as balance for independent variation of pH_2, pH_2O, pCO and pCO_2 respectively. High contents of water vapor were realized by feeding oxygen and hydrogen into an upstream combustion chamber. A Nernst probe located near the sample monitors the pO_2 and hence provides information about the actual gas composition and possible leakages in the setup, which were very low (< 0.02 %).

For the electrochemical characterization, impedance spectra and current voltage characteristics were recorded over an extended range of gas composition (in H_2-H_2O atmosphere: $8 \cdot 10^2$ Pa $\leq pH_2 \leq 9 \cdot 10^4$ Pa and $2 \cdot 10^1$ Pa $\leq pH_2O \leq 6 \cdot 10^4$, in CO-$CO_2$ atmosphere: $4.0 \cdot 10^2$ Pa $\leq pCO \leq 5.1 \cdot 10^4$ Pa and $9.5 \cdot 10^2$ Pa $\leq pCO_2 \leq 9.2 \cdot 10^4$ Pa) and temperature (450 °C $\leq T \leq$ 800 °C). The recording of impedance spectra was performed

both by a Zahner IM6 and a Solartron 1260 FRA, in a frequency range of 100 mHz – 1 MHz. Due to the high impedance of the patterned anodes voltage stimulus was chosen instead of current stimulus; the amplitude was 10 mV.

Our previous study showed that three processes are contributing to the overall impedance response (6): besides the targeted charge transfer process of the Ni patterned anode, contributions of gas diffusion and the counter electrode are detected. For the interpretation of impedance spectra, the same equivalent circuit was used. It consists of three RQ elements in series with additional ohmic contributions of electrolyte and measurement setup and an inductive element accounting for the wiring. The line specific charge transfer resistance LSR_{ct} was determined by multiplying the charge transfer resistance obtained from an equivalent circuit fit with the actual length of the three phase boundary l_{TPB} of the sample.

Temperature-Programmed Desorption and Reaction

In order to obtain thermodynamic and kinetic parameters of CO adsorption/desorption and oxidation on individual Ni and YSZ and H_2 oxidation on YSZ surfaces temperature-programmed desorption (TPD) and temperature-programmed reaction (TPR) experiments were performed under molecular flow conditions in a reaction chamber as described in (21). In the CO desorption and oxidation studies a Ni(111) single crystal (purity ~ 99.99%) was used, which was cleaned by reduction in H_2 atmosphere and repeated sputtering (1 keV) cycles followed by annealing cycles, until a sharp (1 x 1) LEED pattern of the bare Ni surface could be observed. For the CO, H_2 oxidation and CO_2, H_2O surface dissociation studies on YSZ, a polycrystalline sample (8.25 mol% Y_2O_3) from Itochu (Tokyo, Japan) was employed.

Modeling

Quantum Chemical Calculations

Quantum chemical calculations based on density functional theory (DFT) were performed to investigate H_2, CO oxidation and H_2O, CO_2 dissociation energetics on YSZ surfaces. The present calculations were performed using the CASTEP (Cambridge Sequential Total Energy Package) code (22) in the framework of the generalized gradient approximation (GGA), as proposed by Perdew et al. (23), in combination with Vanderbilt ultrasoft pseudopotentials (24). In the computations the plane wave basis set was truncated at a kinetic energy of 420 eV. The calculations were conducted over a range of k-points within the Brillouin zone as generated by the full Monkhorst-Pack scheme (25) with a 2×2×1 mesh. The slab used in this study and the possible reaction pathways of H_2 and CO oxidation are described in detail in Ref. (26).

Elementary Kinetic Modeling

The patterned electrodes were represented in a one-dimensional reaction-diffusion model. The main model assumptions are: i) Electrochemical reactivity is described by elementary kinetics, that is, by resolving single steps that represent chemical reactivity on a molecular scale. The models are thermodynamically consistent by using reversible reactions throughout. ii) The charge-transfer reaction is assumed to be a surface spillover

reaction taking place at the TPB. iii) Surface diffusion is modeled in one dimension perpendicular to the TPB on the basis of a surface-adapted Fickian diffusion approach. The modeling methodology and mathematical equations are described in detail in (27), the model parameters are given in (8). The detailed model comes at the cost of a large number of model parameters (thermodynamic, kinetic and diffusion coefficients of all surface species and surface reactions). Parameter values are obtained using hierarchical approach (16) by combining literature data (both theoretical and experimental) (27) and our own TPD/TPR experiments and DFT calculations. The kinetic coefficients of the spillover reactions were obtained by fitting to our experimental electrochemical data. All simulations were carried out within the in-house software code DENIS (28).

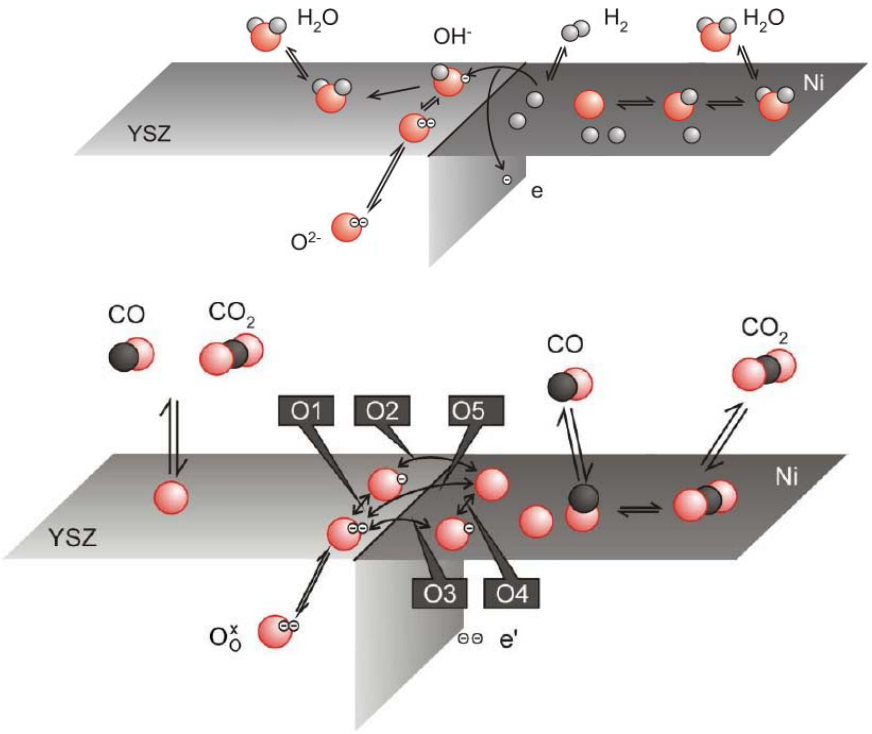

Figure 1. Elementary kinetic mechanisms used in the present work. Upper figure: H_2 oxidation via hydrogen spillover pathway. Lower figure: CO oxidation via combined oxygen spillover and reactive electrolyte pathways.

A number of different spillover scenarios were studied both for H_2 oxidation (including hydrogen spillover, oxygen spillover, hydroxyl spillover hydrogen interstitial pathways) and CO oxidation (including oxygen spillover and reactive electrolyte pathways) (16). In the present paper we show results from selected mechanisms as depicted in Figure 1.

Models for Cermet Anodes

To compare the electrochemical performance of patterned Ni anodes and technical Ni/8YSZ cermet anode, two different models for Ni/YSZ cermet anodes have been parameterized with the LSR_{ct}-values of patterned nickel anodes evaluated in this study: (i) a homogenized transmission line model from (20),(7) and (ii) a space resolved FEM microstructure model (29).

Results and Discussion

Processing and Microstructural Characterization

As pointed out in (6) pre-test SEM analysis showed a perfect pattern, e.g. the stripes exhibited a good adhesion and a straight border, were free of holes and bubbles and no stripes were destroyed or delaminated. Unfortunately these perfect patterns are not stable. During the first 20 h of thermal exposure at 800 °C an initial decrease of the resistance by 60 % to an average LSR_{ct}-value of 54 Ω·m is observed. SEM studies revealed an increase in l_{TPB} of 30 % caused by the grain growth and related morphological changes in the Ni thin film. For the further LSR_{ct}-calculation, this initial increase in tpb-length was considered by a correction factor τ_{corr} = 1.3. The validity of this factor throughout the hole measurement was confirmed by post test analysis of different samples after several hundred hours of testing (18). During the tests no further grain growth occurred and the pattern neither showed delamination nor island, hole or bubble formation as discussed in (5,30).

The initial LSR_{ct}-decrease of 60% during the first 20 h obviously does not match the increase in l_{TPB} of 30%. The microstructural changes are responsible for an apparent LSR_{ct}-decrease of approximately 25%, the remaining 35% have to be attributed to another reason as for example the impurity content at the TPB.

As the initial microstructural changes are unavoidable and reproducible (6), an initial annealing procedure in the test setup (in our case 24 h at 800°C in 90% H_2 / 10% H_2O) resulting in a patterned Ni anode with a sufficient microstructural stability should be considered as the last step in the fabrication procedure. All the LSR_{ct}-values presented in this paper have been measured after the annealing procedure.

Electrochemical Characterization

The aim of the electrochemical characterization was to evaluate reproducible LSR_{ct} values as a function of gas composition and temperature required for elementary kinetic modeling as well as for homogenized and microstructurally resolved modeling of cermet anodes. Our previous studies (6,17,31) showed that next to changes during the initial annealing procedure further dynamic processes with slow settling times have a significant impact on the obtained LSR_{ct} values:

- A degradation rate depending on the gas constituents was observed. A value of 0.4 % / h was determined for a high water vapor content ($pH_2 = 3.9 \cdot 10^4$ Pa, $pH_2O = 6.2 10^4$ Pa) at 800°C. In CO-CO_2 atmosphere, a lower degradation rate of 0.18% was observed. This degradation rate is orders of magnitude higher than the degradation of technical cermet anode structures (32). It is assumed that the degradation is related to an enhanced agglomeration of impurities at the TPB.
- A slow relaxation process after variations of pH_2 and pH_2O was discovered. For pH_2O variations, settling times are 2 ... 3 h at 800°C, while pH_2 variations necessitate longer settling times of 5 ... 8 h at 800°C. For CO-CO_2 atmosphere, equilibrium values were attained within a few minutes. Therefore, it is assumed that this behavior is related to variations in hydrogen concentration in the bulk of electrode and electrolyte.

- A reproducible sequence of fast activation of cell performance during the recording of CV-characteristics followed by a slow relaxation process with settling times of about 20 h is observable.

In order to assure the reproducibility of characterization results, next to the standardized initial heat treatment, a sufficient delay (several hours) between parameter variation and measurement was applied. The fast degradation of the patterned Ni-anodes was considered by periodical EIS-measurements at fixed operating conditions and an appropriate correction of the results. Hence, this is a significant improvement compared to previous studies on patterned Ni anodes, which did neither report these dynamic changes, nor specify the entire measurement procedure.

The parameter dependencies of LSR_{ct} on pH_2, pH_2O, pCO, pCO_2, T and polarization voltage η have been determined by variation of a single parameter at a time. For the recording of measurement series, sufficient settling times have been applied to assure stable conditions. In addition to the detailed elementary kinetic models, we derived empirical global rate laws from the experiments. The dependencies are described in accordance to Butler-Volmer equation using a power law ansatz for the gas composition dependencies and an Arrhenius-type temperature dependency (6,11). The obtained parameters are summarized in Table I.

$$LSR_{ct} = c_1 \cdot \left(pH_{2,An}\right)^{-a} \cdot \left(pH_2O_{An}\right)^{-b} \quad [1]$$

$$LSR_{ct} = c_2 \cdot \exp\left(\frac{E_{act}}{kT}\right) \quad [2]$$

$$LSR_{ct} = c_3 \cdot \left(pCO\right)^{-c} \cdot \left(pCO_2\right)^{-d} \quad [3]$$

$$LSR_{ct} = c_4 \cdot \exp\left(\frac{E_{act,ct}}{RT}\right) \quad [4]$$

TABLE I: Comparison of the parameter dependencies a, b, c and d (all at 800 °C and OCV) and E_{act} obtained for LSR_{ct} of patterned Ni anodes, as reported in our previous studies (6,11). a, b, c and d refer to the dependencies of the resistance on pH_2, pH_2O, pCO and pCO_2 described by $LSR_{ct} \approx pH_2^{-a} \cdot pH_2O^{-b}$ and $LSR_{ct} \approx pCO^{-c} \cdot pCO_2^{-d}$ respectively.

Parameter dependency	Range	LSR_{ct}
a [-]	$pH_2O = 6.7 \cdot 10^3$ Pa:	0.07
b [-]	$pH_2 = 9.0 \cdot 10^3$ Pa:	0.68
$E_{act}(H_2\text{-}H_2O)$ [eV]	700 - 800°C: 450 - 700°C:	1.01 1.37
c [-]	$pCO_2 = 5.1 \cdot 10^4$ Pa: $pCO_2 = 2.0 \cdot 10^4$ Pa:	0.24 0.11 (kink at 10^4 Pa: +0.47 to -0.34)
d [-]	$pCO = 3.9 \cdot 10^4$ Pa: $pCO = 1.0 \cdot 10^4$ Pa:	0.79 0.61(kink at $2 \cdot 10^4$ Pa: +0.76 to +0.42)
$E_{act}(CO\text{-}CO_2)$ [eV]	700 - 800°C:	1.42

In Figure 6 the major results and dependencies are displayed. The evaluated LSR_{ct} values for H_2-H_2O and CO-CO_2 atmosphere are in the same range, which is in good agreement with our results on cermet anodes (33,34). The difference in LSR_{ct} respectively ASR for H_2 and CO electrooxidation is fairly below previously reported values (35),(36). Strong negative dependencies of LSR_{ct} on the reaction product (H_2O and CO_2 respectively) were observed, whereas the dependencies on the reactants (H_2 and CO respectively) are weak. In CO-CO_2 atmosphere, the change in dependency on pCO at ca. 10^4 Pa together with an increase in the activation energy from 0.85 to 1.42 eV is a strong indicator for a change in the reaction mechanism.

The comparison to experimental data with patterned Ni anodes from other groups showed significant deviations in absolute values of LSR_{ct} of up to two orders of magnitude (6), whereas the comparison to point anodes shows weaker deviations within one order of magnitude. This emphasizes the importance of (i) avoidance of impurities and (ii) consideration of dynamic anode processes during the electrochemical characterization.

Impurity Analysis

Whereas the investigation of patterned anodes after electrochemical testing (> 200 h @800 °C) by TEM revealed no impurity agglomeration at the TPB (Figure 3), SEM analysis showed nanoscaled imprints on the electrolyte surface close to the TPB (Figure 3). Compared to the SiO_2-based impurity ridges discussed in literature (37), which exhibited a height of up to several µm, the "impurity imprints" in our study were orders of magnitude smaller.

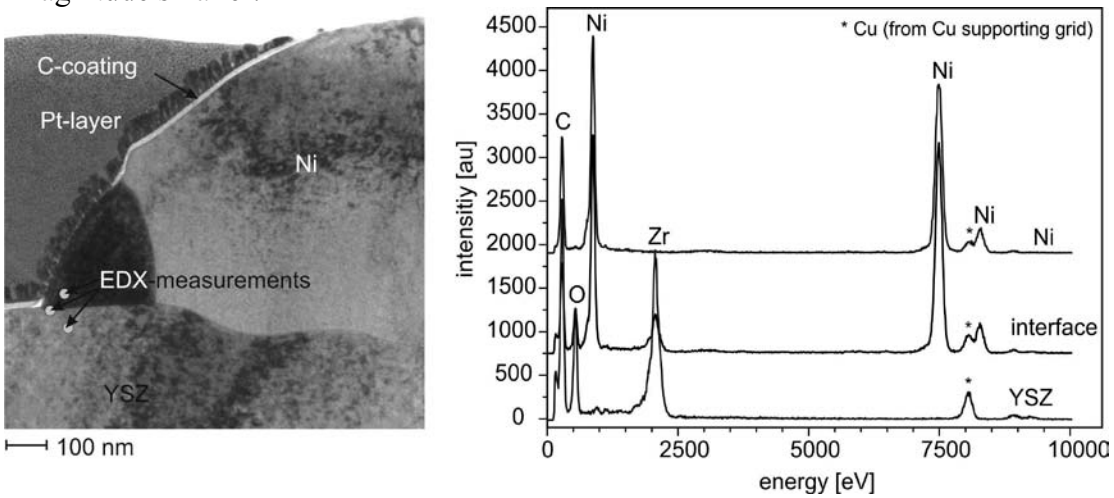

Figure 2. TEM cross section image of the TPB; the EDX measurements at the TPB showed the existence of nickel, yttria and zirconia only.

The "impurity imprints" observed in the SEM were confirmed by the AFM analysis. The height was in the range of 8 to 15 nm. Each individual imprint is about 10 to 30 nm wide, whereas the whole area covered by these imprints did not exceed 2 µm. A space resolved chemical analysis of the imprints, with a height of less than 40 atomic layers (assuming that the impurity consists of SiO_2), was not possible so far. The TOF-SIMS and XPS analysis only provide space resolutions of several 100 nm and several 100 µm respectively. Therefore no information about the composition of the imprints is available

up to now. The TOF-SIMS analysis (Figure 4) shows the lateral distribution of the main impurities. It is obvious, that there is no detectable enrichment of SiO_2 at the TPB but Ca and Mg show an increase in intensity close to the Ni electrode. This might indicate species accumulation at the impurity imprints, however the lateral extension of approximately 4 µm is rather large compared to 1 ... 2 µm width of the area covered with the imprints.

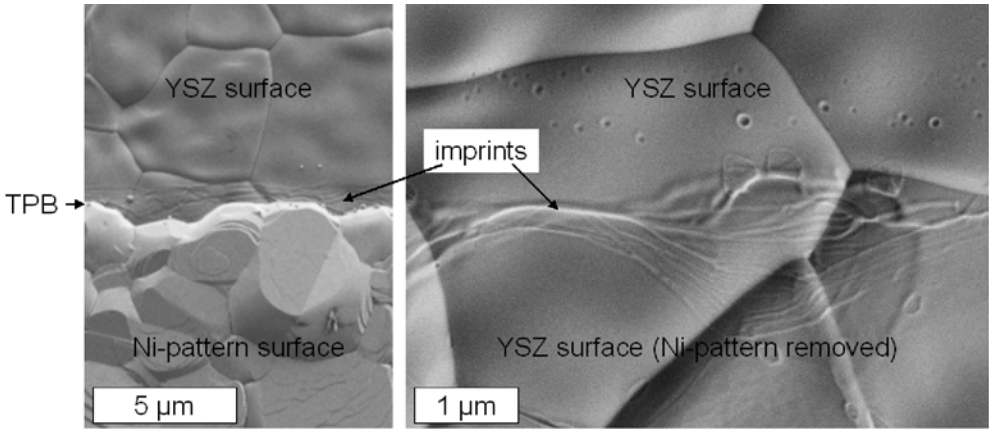

Figure 3. SEM images showing nanoscaled imprints on the electrolyte surface close to the TPB.

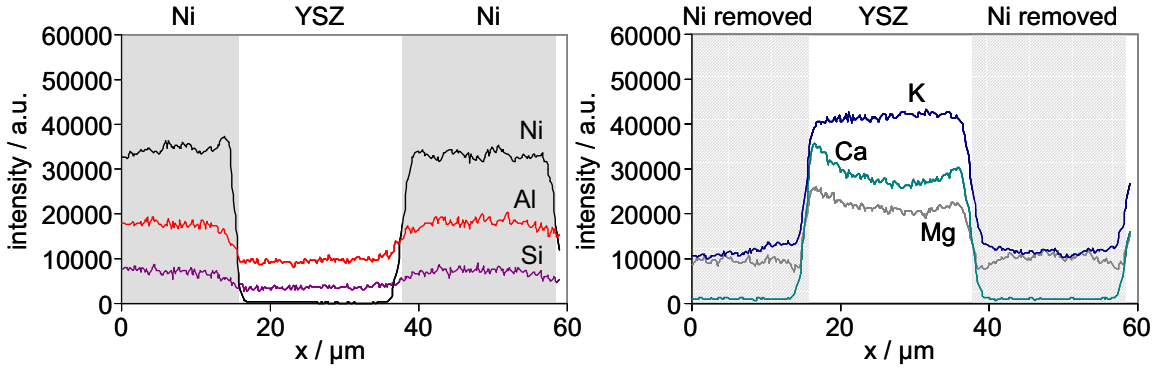

Figure 4. TOF-SIMS intensity profile taken from a 60 x 60 µm² scan of main impurities on the sample with Ni pattern (right) and after removing the Ni-pattern (left). The Ni signal is plotted for comparison.

Whereas TOF-SIMS can not provide accurate information about the concentration of the different impurities, the XPS-analysis showed that the amount of impurities and especially the amount of Si on the surface of the samples in this study is very low (sum of impurities/Zr = 0.25 - 0.28, Si/Zr = 0.025 - 0.173) compared to values for highly pure point electrodes reported in literature (sum of impurities/Zr = 0.54, Si/Zr = 0.35) (19), (14). Comparing the nominal silica content in the YSZ-substrate (0.032 wt.% SiO_2) and the Si/Zr ratios on the substrate surface of 0.173 (as delivered), 0.118 (after sintering of the counter electrode at 1300 °C) and 0.025 (after characterization), it is obvious that the silica is accumulated at the YSZ-surface during high temperature treatment. Despite that the SiO_2-content of the Ni-target is 3 times lower (< 0.01 wt.%), the TOF-SIMS analysis shows a higher amount of silica on the Ni-surface. We assume that the redistribution of impurities during the initial annealing at 800 °C and the following testing period influences the dynamic change of the LSR_{ct} significantly (14).

Quantum Chemical Calculations

The low-energy surface reaction pathways for H_2 and CO oxidation at YSZ surface, as obtained in the DFT calculations, are depicted in Figure 5. Both reaction pathways, I and II, lead to the formation of gaseous H_2O and CO_2 products, respectively. H_2O formation, however, proceeds via H_2 dissociative adsorption - resulting in surface OH species formation - followed by a surface H_2O formation step (see Figure 5.I, second and third structures) via a Langmuir-Hinshelwood (LH) reaction mechanism. On the other hand, as indicated by the DFT results shown in Figure 5.II (38), in mutual agreement with recent experimental studies (21), gaseous CO_2 is formed via an Eley-Rideal mechanism in which a gas phase CO molecule directly reacts with a surface oxygen atom to form CO_2, which then readily desorbs into the gas phase. The activation energies obtained in the DFT calculation were used in the simulation of TPD/TPR spectra measured for H_2 and CO oxidation over YSZ (for details see e.g. Ref. (26) and (38)).

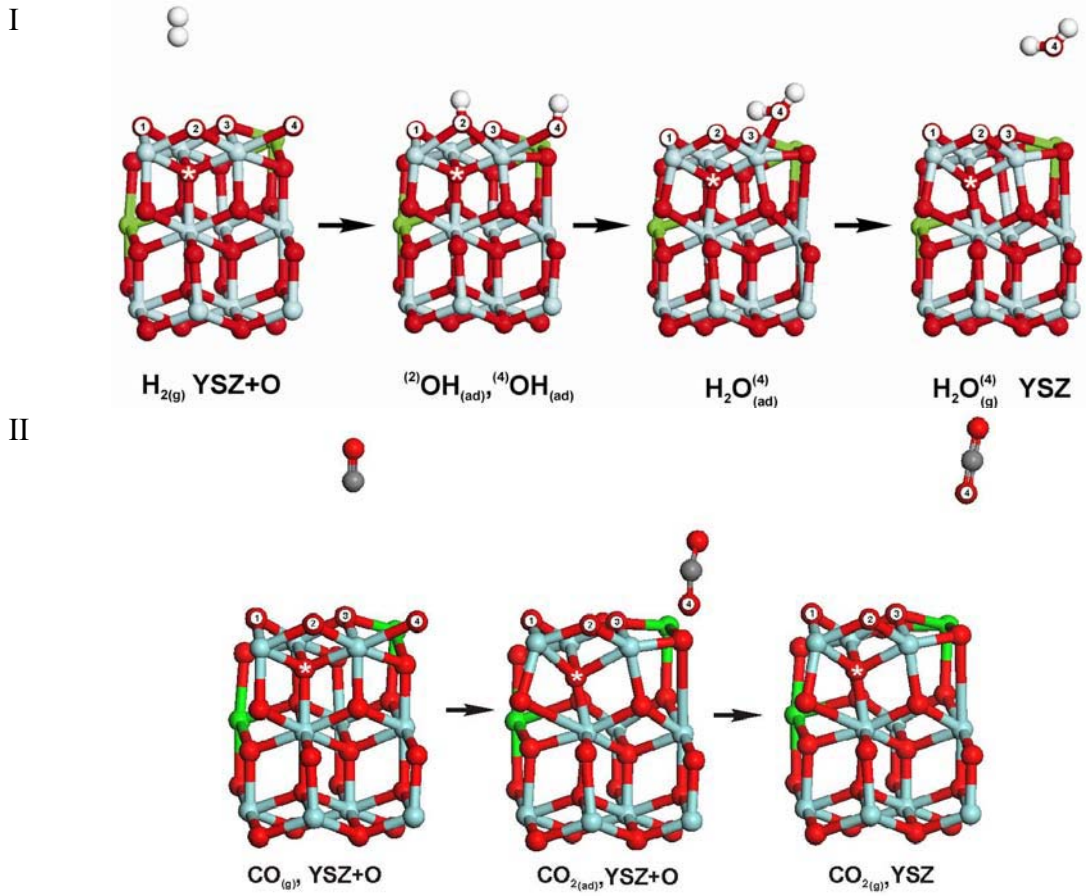

Figure 5. Illustration of surface reaction pathway as obtained in the DFT studies [10] of heterogeneous H_2 and CO oxidation on YSZ surfaces.

Heterogeneous Chemistry of H_2/H_2O and CO/CO_2 on Ni and YSZ

CO TPD and CO/CO_2 TPR experiments along with numerical simulations allowed to determine quantitative CO adsorption/desorption and CO oxidation surface reaction kinetics parameters (21). The CO oxidation studies over YSZ along with DFT calculations revealed that CO_2 formation can proceed via a so far unknown Eley-Rideal mechanism where CO_2 is formed by direct reaction of gas phase CO molecules with O-atoms of the YSZ surface. In addition, TPR and TPD studies of H_2 oxidation and H_2O

dissociative adsorption along with DFT calculations and numerical simulations of the experimental spectra allowed the development of a revised H_2/H_2O/YSZ adsorption/desorption and surface reaction mechanism along with the necessary experimentally validated kinetics data set. The experimental studies further demonstrated that during H_2 oxidation and H_2O dissociative adsorption noticeable amounts of H_2O are "dissolved" in the YSZ bulk, either as interstitial protons (hydrogen) or interstitial OH. The latter result, points towards the possibility of an alternative charge transfer mechanism in the electrochemical H_2 oxidation on Ni-pattern/YSZ anodes, which might involve interstitial OH and/or proton transport through the electrolyte to the Ni electrode with the actual charge transfer taking place at the Ni-bulk-YSZ-bulk two-phase boundary (26,39).

Elementary Kinetic Modeling of the Electrochemical H_2 Oxidation

Previous studies on model anodes have shown that gas-phase composition and temperature have a strong influence on electrode kinetics (8). Experimental and simulation results of pH_2, pH_2O and temperature variations are shown in Figure 6 a,b,c. It is obvious that pH_2 has only a weak influence on the LSR_{ct}. Experimentally, it appears that at low pH_2O, LSR_{ct} slightly increases with increasing pH_2, while the trend is inverse at higher pH_2O. The simulation is in agreement with the experiment at high pH_2O. Although the slope of the simulation is somewhat smaller for low pH_2O, the experimental trend is not completely reproduced. An increase in pH_2O strongly enhances electrode performance. The variation of pH_2O over three orders of magnitude leads to a variation of LSR_{ct} of around two orders of magnitude. The simulation is in excellent agreement with the experiment for both pH_2 shown. The trend that we observe here was found in the same way in the pattern anode studies of Bieberle et al. (1) and Mizusaki et al. (3); a more detailed comparison is given in (6).

This observed gas-composition dependence of the LSR_{ct} is counter-intuitive. Water is a reaction product; according to the principle of Le Chatelier, an increase in product concentration should decrease the reaction rate, while here we observe the opposite. However, the Le Chatelier principle in this simple form is only true for a purely chemical system where reaction rates are indeed only influenced by concentration. In an electrochemical system, such as an SOFC electrode, reaction rates are additionally (and even dominantly) influenced by the electrode potential. A variation in gas-phase composition changes both, the concentrations of the adsorbed intermediates participating in the charge-transfer reaction, and the electrode potential (which can be described by the Nernst equation). The combined concentration and potential changes lead to the observed counter-intuitive change in macroscopic electrode performance which is accurately described by our model. Experimental and simulated LSR_{ct} values are plotted as a function of temperature in Figure 6c.

In the present experiments, temperature was varied over the wide range of 673-1073 K. Two regimes with slightly different activation energies above and below ca. 950 K become apparent (cf. also (6)). The simulations are in good agreement with the experiments. The observation of two regimes is reproduced in the simulations, yet the change in activation energy seems to be overpredicted.

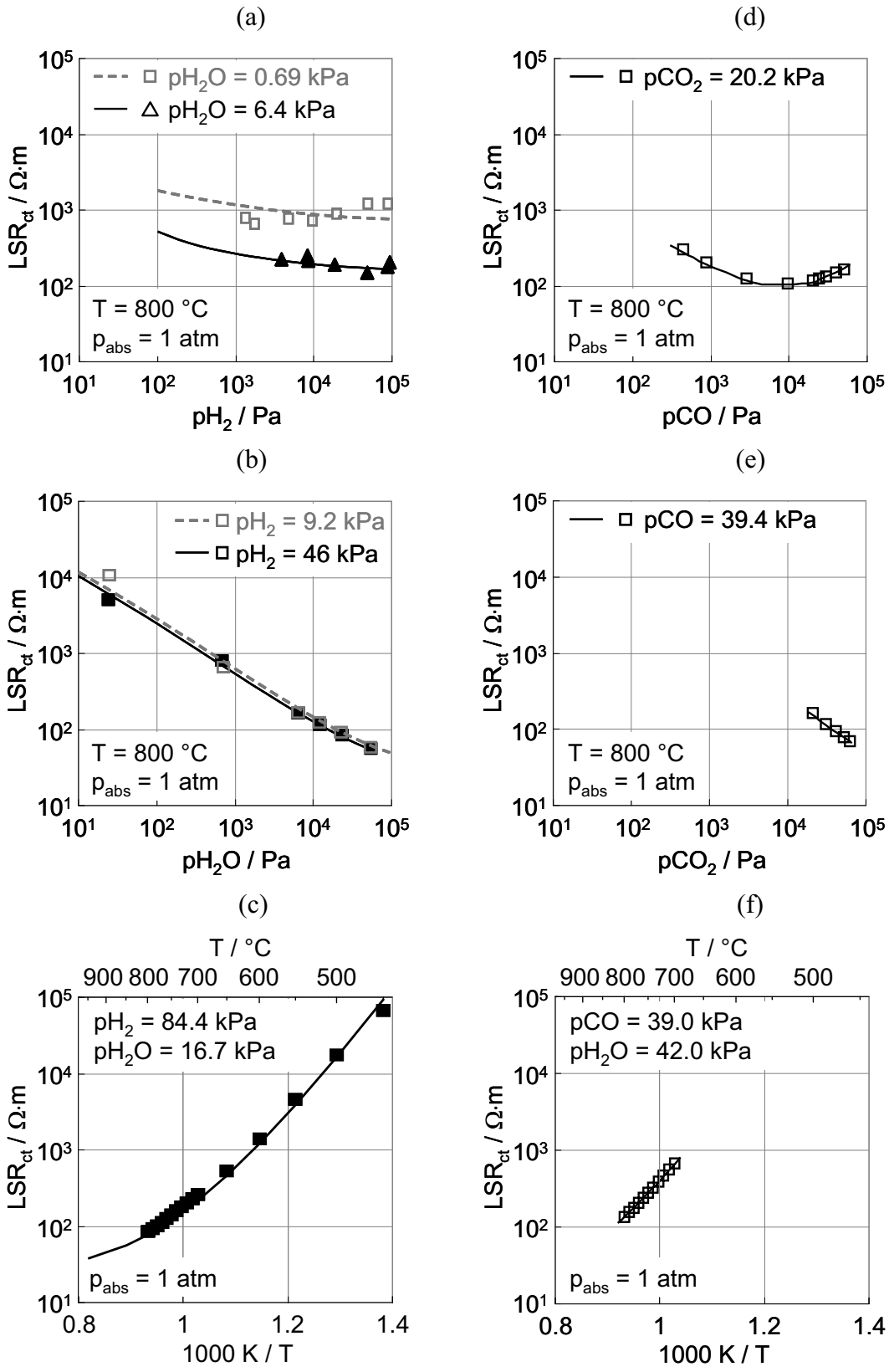

Figure 6. Experimental (symbols) and simulated (lines) line-specific resistance (LSR_{ct}) as a function of partial pressure of oxidizable compounds (H_2 / CO), reaction products (H_2O / CO_2) and temperature.

In order to further interpret the behavior, a sensitivity analysis was performed for two different temperatures. In such an analysis, model parameters P are individually varied by 20 %, and the impact on the LSR_{ct} is quantified as dimensionless relative sensitivity, $s = (\Delta LSR_{ct} / LSR_{ct})/(\Delta P/P)$. A sensitivity of unity means that the system's LSR_{ct} responds linearly with a change of parameter P. A sensitivity close to zero means that the physical process that is described by the parameter (e.g., diffusion coefficient, rate coefficient) does not influence the LSR_{ct} and is therefore not rate-determining. Results for T = 773 K and 1173 K are shown in Figure 7. The data are separated into kinetic parameters of all reactions (pre-exponential factors), transport parameters of all surface-adsorbed species (diffusion coefficients), thermodynamic parameters of selected species (chemical potential) and other parameters (pressure, TPB, temperature). At 773 K, the only rate-determining reaction is one charge-transfer reaction (spillover of hydrogen from the Ni surface to hydroxyl ions on the YSZ surface, yielding YSZ-adsorbed H_2O). At 1173 K, this reaction is co-limited by the other charge-transfer reaction (spillover of hydrogen from the Ni surface to oxygen ions on the YSZ surface) as well as the water dissociation and water desorption reactions on YSZ. This change in rate-determining steps is the origin of the observed change in activation energy.

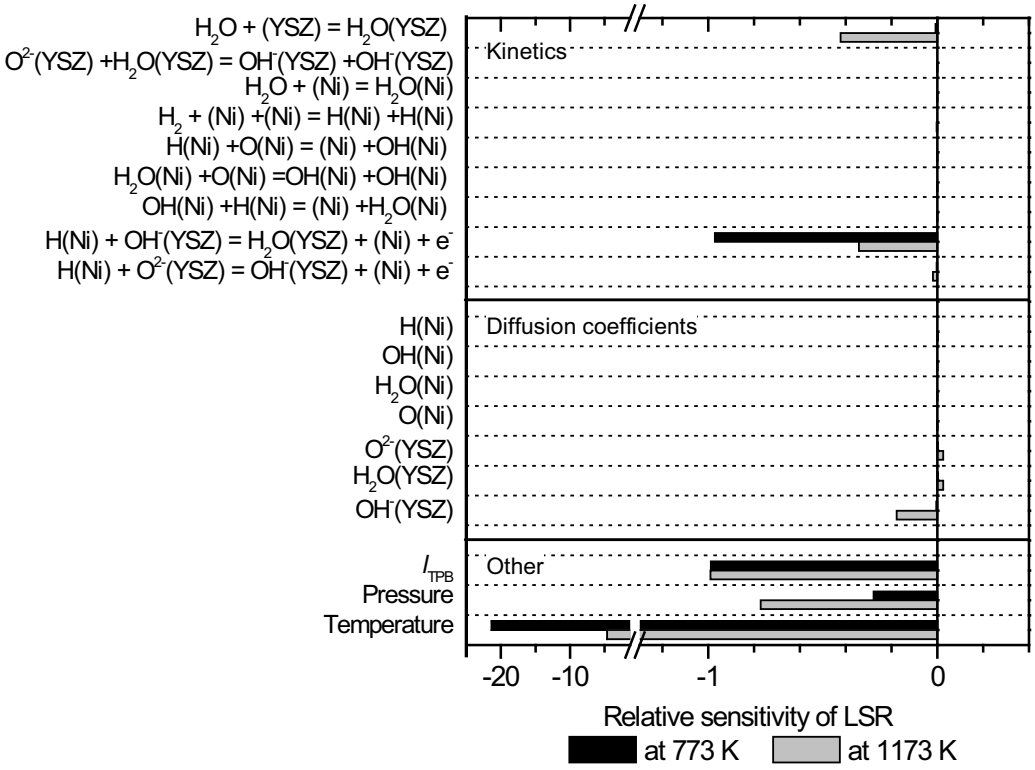

Figure 7. Sensitivity analysis for the pattern anode performance (line-specific resistance) for two different temperatures (η = 0 V, $pH_2 = 8.44 \cdot 10^4$ Pa, $pH_2O = 1.67 \cdot 10^4$ Pa). A positive value for the sensitivity means that an increase in parameter increases the LSR_{ct}.

Electrochemical CO Oxidation

Experimental and simulated LSR_{ct} as function of CO and CO_2 partial pressure and temperature in the $CO/CO_2/N_2$ system is shown in Figure 6d,e,f. The simulations are based on a reaction mechanism consisting of three distinct CT steps denoted in the following as O1, O2, and O6 (Figure 1). In the first CT step, an electron is transferred to

the Ni electrode O1: ($O^{2-}_{YSZ} \rightleftharpoons O^{1-}_{YSZ} + e^{-}_{Ni}$). This CT step is followed by two competitive CT steps (O2 and O6). O2 represents an oxygen ion spillover reaction with a simultaneous discharge of the oxygen ion, O2: ($O^{1-}_{YSZ} + \square_{Ni} \rightleftharpoons O_{Ni} + \square_{YSZ} + e^{-}_{Ni}$), and O6 represents a simple electron transfer step O6: ($O^{1-}_{YSZ} \rightleftharpoons O_{YSZ} + e^{-}_{Ni}$) in which a YSZ surface oxygen ion transfers an electron to the Ni electrode. The pronounced minimum in the CO pressure dependence of the line-specific resistance can be explained in a straightforward way in the framework of this mechanism. In the region of high CO pressure, the O2 CT step is dominating, with decreasing CO partial pressure, which results in a pronounced increase of the oxygen coverage of the Ni TPB region, the overall mechanism changes and the O6 CT steps starts to become rate determining (40).

Applicability of Patterned Anode Results in Cermet Anode Models

One major question concerning model anodes is, if the evaluated LSR_{ct} values agree with the LSR_{ct} at the TPB in cermet anodes. A first comparison of the electrochemical performance of patterned Ni anodes and technical Ni/8YSZ cermet anodes has been performed by a theoretical calculation of the ASR of a cermet anode based on LSR_{ct} values from patterned Ni anodes. Using available models as the transmission line model with homogenized electrochemical and transport properties (20) and the space resolved FEM-model with a simplified microstructure (29) good agreement between the performance of a Ni/8YSZ cermet anode and the simulations using the LSR_{ct} values obtained with patterned Ni anodes was found (41).

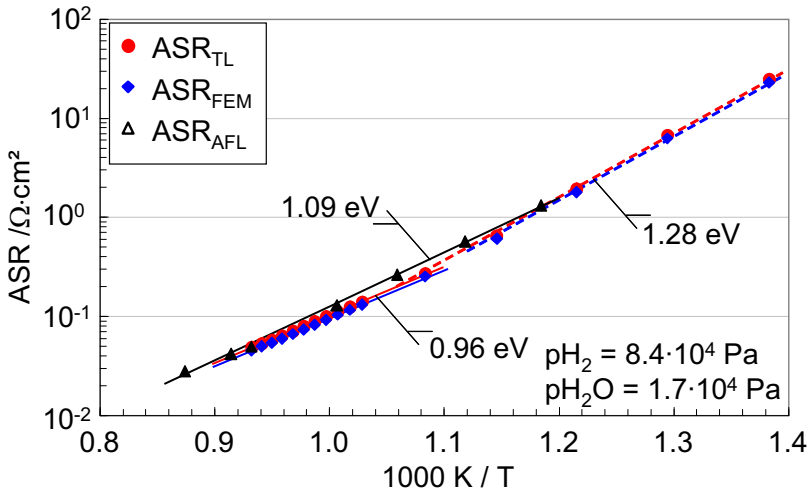

Figure 8. Comparison of results from transmission line calculation ASR_{TL} and microstructure simulation ASR_{FEM} to ASR values of the Ni/8YSZ cermet anode ASR_{AFL}.

The comparison indicated that in case of H_2-H_2O similar reaction mechanisms take place in both anode concepts, whereas for CO-CO_2 deviations concerning the p(CO_2)-dependency were observed. These deviations can be related to a different electrochemical behavior resulting from impurities (14) aging and other dynamic effects as discussed in (6). In comparison with Ni/8YSZ-cermet anodes (32), even microstructurally stable model anodes showed a more distinctive dynamic behavior and an approximately 3 orders of magnitude higher degradation rate (6,11). Further investigations concerning these dynamic processes at model anodes and a comparison with cermet anodes are

expected to provide a detailed understanding of the degradation processes taking place at the TPB and might even help to predict the long term degradation of cermet anodes.

Conclusions

The combination of experimental investigations of patterned nickel anodes and modeling provided a profound understanding of the elementary kinetics of the electrooxidation of hydrogen and carbon monoxide at the three phase boundary nickel / 8YSZ / fuel gas.

The line specific resistance of the three phase boundary was evaluated within a wide range of gas compositions and temperature. The investigations showed that microstructural stability, impurities, accelerated degradation and reversible dynamic changes are key issues which have to be considered. Applying samples and test setups with a sufficient purity as well as appropriate annealing and testing conditions, the line specific resistance can be evaluated with a high reliability.

The comparison of the electrochemical results and elementary kinetic simulations of different spillover scenarios for H_2 and CO oxidation revealed that H_2 is primarily electrooxidized via a hydrogen spillover whereas for CO the electrooxidation occurs via a combined oxygen spillover and reactive electrolyte pathways. For these elementary kinetic mechanisms the models, parameterized with literature data, temperature-programmed desorption and reaction and quantum chemical calculation results were in excellent agreement with the experimental data.

For the first time LSR_{ct} values evaluated by means of patterned anodes have been applied in homogenized and space resolved models for cermet anodes. The good agreement of modeling and experimental results proved that similar reaction mechanisms take place in both anode concepts and that the results of patterned anode studies can be transferred to cermet anode structures.

Acknowledgments

Funding of this work was provided by the German Research Foundation (DFG) under grants no. BE 3819/1-1, VO 642/2-1, GE 841/15-1, WE 4188/1-1 and IV 14/16-1. KIT acknowledges further support from the Friedrich-und-Elisabeth-BOYSEN-Stiftung. WGB acknowledges support from the Initiative and Networking Fund of the Helmholtz Association.

References

1. A. Bieberle et al., *J. Electrochem. Soc.*, **148**, A646 (2001).
2. B. de Boer, PhD Thesis, University of Twente, The Netherlands (1998).
3. J. Mizusaki et al., *Solid State Ionics*, **70**, 52 (1994).
4. J. Mizusaki et al., *J. Electrochem. Soc.*, **141**, 2129 (1994).
5. A. M. Sukeshini et al., *J. Electrochem. Soc.*, **153**, A705 (2006).

6. A. Utz et al., *J. Electrochem. Soc.*, **157**, B920 (2010).
7. A. Leonide et al., *Proceedings of the 8th European Solid Oxide Fuel Cell Forum*, A0501 (2008).
8. W. G. Bessler et al., *Physical Chemistry Chemical Physics*, 10.1039/C0CP00541J, 13888 (2010).
9. A. Utz et al., *Proceedings of the 9th European Solid Oxide Fuel Cell Forum*, 5-91 (2010).
10. F. Z. Boulenouar et al., *ECS Trans.*, 2001, 759 (2001).
11. A. Utz et al., *J. Power Sources*, 10.1016/j.powsour.2010.10.056 (2010).
12. M. Mogensen et al., in *Handbook of Fuel Cells - Fundamentals, Technology and Applications*, W. Vielstich, H. Yokokawa, and H. A. Gasteiger (Eds.), p. 543, John Wiley & Sons Ltd, Chichester (2009).
13. S. B. Adler, *J. Electrochem. Soc.*, **149**, E166 (2002).
14. A. Utz et al., *Solid State Ionics*, accepted for publication, (2010).
15. M. Shishkin et al., *Journal of Physical Chemistry C*, **113** (2009).
16. S. B. Adler et al., 5 ed., W. Vielstich, H. Yokokawa, and H. A. Gasteiger (Eds.), John Wiley & Sons, Chichester, UK (2009).
17. A. Utz et al., *Solid State Ionics*, accepted for publication, (2010).
18. H. Störmer et al., *Proceedings of the 9th European Solid Oxide Fuel Cell Forum*, 5-122 (2010).
19. K. Norrman et al., *Journal of the European Ceramic Society*, **26**, 967 (2006).
20. V. Sonn et al., *J. Electrochem. Soc.*, **155**, B675 (2008).
21. V. Yurkiv et al., *J. Electrochem. Soc.*, **158** (2010).
22. M. D. Segall et al., *J Phys-Condens Mat*, **14** (2002).
23. J. P. Perdew et al., *Phys Rev B*, **46** (1992).
24. D. Vanderbilt, *Phys Rev B*, **41** (1990).
25. H. J. Monkhorst et al., *Phys. Rev. B*, **13** (1976).
26. A. Gorski et al., *J. Power Sources*, **in press** (2010).
27. M. Vogler et al., *J. Electrochem. Soc.*, **156**, B663 (2009).
28. W. G. Bessler et al., *Electrochim. Acta*, **53** (2007).
29. B. Rüger et al., *Proceedings of the 7th European Solid Oxide Fuel Cell Forum*, B075 (2006).
30. A. Ehn et al., *J. Electrochem. Soc.*, **157**, B1588 (2010).
31. A. Utz et al., *ECS Trans.*, **25**, 2013 (2009).
32. C. Endler et al., *J. Electrochem. Soc.*, **157**, B292 (2010).
33. A. Leonide et al., *J. Electrochem. Soc.*, **155**, B36 (2008).
34. A. Leonide et al., *J. Power Sources*, **in press** (2011).
35. R. J. Aaberg et al., *Proceedings of the 17th Risoe International Symposium on Materials Science: High Temperature Electrochemistry: Ceramics and Metals*, 511 (1996).
36. P. Holtappels et al., *Journal of Applied Electrochemistry*, **29**, 561 (1999).
37. K. V. Jensen et al., *Solid State Ionics*, **160**, 27 (2003).
38. A. Gorski et al., *ECS Trans.* (2011).
39. M. Vogler et al., *ECS Trans.*, **25** (2009).
40. V. Yurkiv et al., *these proceedings,* (2011).
41. A. Utz et al., *these proceedings,* (2011).